Intrinsic Q_p seismic attenuation from rise time of microearthquakes. A local scale application at Rio-Antirrio W.Greece.

G-Akis Tselentis[1]*, Paraskevas Paraskevopoulos*[1]*, and Nikos Martakis*[2]

(1)University of Patras Seismological Lab; (2)LandTech Enterprises

Email:tselenti@upatras.gr

ABSTRACT

We determine attenuation structure of a three-dimensional medium based on first pulse-width measurements from microearthquake data. Ninety five microearthquakes from a seventy stations local network were considered in this study. Measurements of the first half cycle of the wave, the so-called rise time τ were carried out on high quality velocity seismograms and inverted to estimate the P-waves intrinsic quality factor Q_p. The results of this investigation indicate that first pulse width data from a local microearthquake network permit retrieval with sufficient accuracy of the heterogeneous Q_p structure. The inferred attenuation variability corresponds to the known geological formations in the region.

Key words: Intrinsic quality factor.

Intrinsic Q_p seismic attenuation from rise time of microearthquakes. A local scale application at Rio-Antirrio W.Greece.

G-Akis Tselentis[1]*, Paraskevas Paraskevopoulos*[1]*, and Nikos Martakis*[2]

(1)University of Patras Seismological Lab; (2)LandTech Enterprises

ABSTRACT

We determine attenuation structure of a three-dimensional medium based on first pulse-width measurements from microearthquake data. Ninety five microearthquakes from a seventy stations local network were considered in this study. Measurements of the first half cycle of the wave, the so-called rise time τ were carried out on high quality velocity seismograms and inverted to estimate the P-waves intrinsic quality factor Q_p. The results of this investigation indicate that first pulse width data from a local microearthquake network permit retrieval with sufficient accuracy of the heterogeneous Q_p structure. The inferred attenuation variability corresponds to the known geological formations in the region.

Key words: Intrinsic quality factor.

INTRODUCTION

Recent advances in seismological instrumentatation, methodologies and inversion algorithms have revealed the potential of applying passive seismic monitoring in the hydrocarbon industry as well. Most of the up-to-date passive applications have been devoted to reservoir monitoring projects, fracture location and orientation. Even though the 3D tomographic velocity inversion in general has been in use for more than 25 years (Thurber 1983) for regional geotectonic investigations, its application to a local scale with possible application in hydrocarbon exploration and engineering projects is relatively recent (Vesnaver *et al.* 2000; Durham 2003; Kapotas Tselentis and Martakis 2003; Vesnaver *et al.* 2003; Martakis Kapotas and Tselentis 2006; Tselentis *et al.* 2007).

One of the geophysical parameters that correlate best to the physical state of the rocks and the fluid percentage is the intrinsic quality factor Q_p of the compressional body waves (Bourbie Coussy and Zinszner 1987). As an exploration tool, attenuation effects have only recently attracted attention (e.g. Hedlin Mewhort and Margrave 2001). Q_p can prove useful in two ways; as a mean of correcting seismic data to enhance resolution of conventional imaging techniques, and as a direct hydrocarbon or geothermal indicator.

Several investigations in geothermal areas (Zucca Hutchings and Kasameyer 1994; Sanders and Nixon 1995; Sanders *et al.* 1995; Wu and Lees 1996; Zollo and de Lorenzo 2001) have shown that the imaging of the quality factor Q is a useful tool to define location and extension of magma bodies in volcanic areas and to detail the fluid contribution through fracture systems. Usually, high degree of cracking or high effective porosity (Zucca *et al.* 1994; Sanders *et al.* 1995) and the presence of water/gas in the fractures lower Q_p values.

The primary mechanisms causing energy loss of seismic waves as they propagate through the earth, are spherical divergence, scattering and intrinsic attenuation. The first mechanism is frequency independent and a correction is commonly applied to seismic data. Scattering is the result of multiples that lag the primary seismic energy and tend to cause partial cancellation of primary seismic energy, it is frequency dependent and difficult to separate from intrinsic attenuation. The latter is the effect of energy loss due to friction and appears to dominate scattering attenuation.

Intrinsic attenuation occurs in porous rocks when motion of the rock and the fluid in the pores becomes uncoupled. The rock becomes anelastic as energy is lost due to fluid friction (Pride *et al.* 2003). If the pore space is completely filled with fluid, the fluid has less mobility than if there is some gas saturation, and is expected that attenuation is higher in a partially fluid saturated rock (Winkler and Nur 1982). Theoretically, a subsurface reservoir full of hydrocarbons will tend to be acoustically “softer” than a porous rock filled only with water (Kumar Batzle and Hofmann 2003).

Until now, most attempts to extract attenuation at a local scale are restricted to active seismic data recorded at the surface (Clawson Smith and. Benz 1989; Evans and Zucca 1988). This approach encounters significant difficulties, because the amplitude spectrum of the seismic record contains the imprint of the amplitude spectrum of the earth’s reflectivity as well as the amplitude spectrum of the seismic wavelet. In the present investigation we will attempt to extract seismic attenuation values from data obtained from a local high density microearthquake network.

Several methods have been developed to compute intrinsic attenuation and have been applied mostly in a regional scale (Ho-Liu Kanamori and Clayton 1988; Sekiguchi *et al.* 1996; Sarker and Abers 1998; Rietbrock 2001). Most of these methods are applied to the frequency domain and are very dependent on source and instrument properties.

Pulse width methods do not require precise measuring of pulse amplitudes or taking into account the instrument response. Unlike spectral methods, the pulse width methods only require a very short part of the first arriving signal, which is relatively free of other interfering waveforms (reflections, scattering, or multiple travel paths).

The early experimental bases of this method have been given in analyses of waveforms from both earthquakes (Okada 1970; O’Neill and Healy 1973), point-like sources (Gladwin and Stacey 1974; Stacey *et al.* 1975; Wright and Hoy 1981) and theoretical studies (Kjartannson 1979). More recently, Wu and Lees (1996) showed that the theoretical relationships on which the method is based remain valid if we consider a heterogeneous anelastic structure.

The method based on the inversion of the rise times is expected to give the most reliable estimates of the intrinsic attenuation (Liu *et al.* 1994). In fact, since only a very limited portion of the seismogram is used, the effects of multiple waves generated in thin layers around the recording site are usually minimized (De Lorenzo *et al*. 2006).

The availability of a high quality set of 3-component digital recordings, obtained from a dense 70-station, microearthquake network at Rio-Antirrio (W. Greece) allow to investigate the attenuation state of this region by performing a tomographic inversion of Q_p employing the pulse width method.

RISE TIME AS A MEASURE OF Q

The pulse rise time is defined as the amplitude of the first arriving pulse divided by the steepest rising slope. The rise time, defined on displacement records, is approximately the pulse width on velocity seismograms (Zucca *et al.* 1994), which is defined as the time difference from onset of initial arrival to initial peak for displacement seismograms, or equivalently, from onset to first zero crossing for velocity records. Since, for short pulse widths, the error introduced by mispicking can be large, we use the time between the intercept of the linear extrapolations of the rising slope at half peak (Figure 1), to the time axis and the first zero crossing (Zucca *et al.* 1994).

A mathematical model for realistic pulse broadening in an inhomogeneous medium has been suggested by Gladwin and Stacey (1974) and Stacey *et al.* (1975). They showed experimentally that the rise times of acoustic signals propagating linearly in elastic media with frequency-independent quality quotient for P waves Q_p is described by the equation

$$\tau = \tau_0 + C\int_{ray}\frac{ds}{V_p Q_p} = \tau_0 + C\int_{ray}\frac{dt}{Q_p} \qquad (1)$$

Where τ is the pulse rise time, τ_o is the original pulse rise time at the source, V_p is the P-wave velocity, C is a constant, ds is an arc segment along ray path and dt is the incremental travel time.

For a medium with constant V_p and Q_p=Q, equation (1) can be written in the following linear form

$$\tau = \tau_0 + \frac{CT}{Q} \qquad (2)$$

The ratio T/Q is usually referred as t* in the literature. The constant C was experimentally determined for ultrasonic acoustic pulses to be equal to 0.5 (Gladwin and Stacey 1974), whereas a theoretical demonstration, based on impulsive displacement source, was given by Kjartansson (1979).

Other investigations (Blair and Spathis 1982; Liu 1988; Wu and Lees 1996; Tselentis 1998) have shown that C depends on the shape of the source time function. For the case of small events a C value of 0.5 corresponding to an impulsive displacement function is commonly used (De Lorenzo *et al.* 2004). This is due to the fact that first arrival velocity pulses for microearthquakes appear closest in shape to Gaussian derivative pulses that correspond to Gaussian function displacements.

Obviously, the most limiting assumption of this method is that it neglects the directivity effect of the seismic radiation generated by a finite dimensional seismic source. (Zollo and De Lorenzo 2001; Tselentis *et al.* 2009). The directionality of the source will have a limited effect as long as it only affects the amplitude of the signal, and not the spectral content. Because of this events of greater magnitude are better been avoided when using this method. In order to limit this effect, relatively small earthquakes were selected and the use of the stronger events was avoided.

DATA

The selected area for the local tomographic Q_p inversion is located around the Rio-Antirrio Strait (Figure 2). A microearthquake network, consisting of 70 Earthdata PR24 recording stations supplemented with LandTech LT- S100 three-component velocity sensors, was deployed during a three month seismic experiment in the autumn of 2004. We attempted to deploy the network over a grid with an average spacing between nodes of 500 m (Figure 2). Station coordinates were established by differential GPS measurements with a horizontal accuracy of ± 2m and a vertical accuracy of ± 1 m. Time sampling was 200 samples per second. The estimated time picking accuracy was between 0.010s and 0.025s in the noisy records for P-waves.

Because of the generally higher amplitude of the vertical component of the first motion, the P-wave rise times were measured on this component. Errors in picking first arrival times do not affect measurements for pulse widths, if the correct initial pulse widths are selected. Systematic measurement errors in pulse width may be absorbed either into the constant C or into source pulse width τ_o (Wu and Lees 1996; Tselentis 1998).

Site effects are often recognized as the cause of secondary arrivals after the first P-wave motion (Figure 3). These arrivals are attributed to the presence of thin layers below the recording site, resulting in the trapping of the wavefield causing multiple reflections. In most cases, multipath effects produce a discontinuity in the observed P-pulse shape (e.g. Deichmann 1999; Courboulex Deichmann and Gariel 1999). In order to avoid these effects in our work, we have discarded the recorded P-wave pulses with a clear discontinuity during the first period of P-motion.

We have also discarded all data for which the P signal to noise ratio was lower than 10, and considered only the waveforms on which the P-wave onset was clearly readable. Taking all the above factors into consideration we selected a subset of 95 from the 220 initially recorded events to be used for the present attenuation investigation (Figure 4).

Figure 5 shows that the rise time increases with the hypocental distance as the slope of the least squares fitting line is different from zero at 0.0028 s/km and the data have a correlation coefficient of ~0.4. This suggests that in the case of this data set the pulse width can be considered a valid model for estimating Q.

Since, the methodology used does not utilize amplitude information we did not perform the deconvolution for the instrument response. Furthermore, an additional check can be done by representing the histograms of the observed rise times and the reduced rise times (Figures 6a, b). Figure 6a shows that the majority of observed rise time values lie between 0.02s and 0.08s, which compared to an average frequency content ranging from 3- 40Hz, a frequency band where the response of the used seismometers is flat and cannot distort the duration and shape of the observed signals.

INVERSION APPROACH

First, we estimate the initial rise time of each event. As each event has different initial rise time τ_0 there will be one τ_0 per event. Then we pick, if possible, the rise time τ for each recorded waveform. We plot for each event the value of the rise times against the P-wave arrival travel times. A straight line is fitted on the data points using the least squares method. The point where the line will intersect with the rise time axis (equation 2) is the value of τ_0 that will be used for that event. An example of this procedure is presented in Figure 7.

Next from equation 1, we can write:

$$\tau - \tau_0 = \mathrm{C}\int_{\mathrm{ray}} \frac{1}{Q_p V_p} ds \tag{3}$$

The term τ-τ_o, is the reduced rise time (also called corrected rise time) and represents the rise time with the effects of the initial pulse at the source, removed.

As it is seen from equation 3, it is important to have an accurate P-wave velocity model $V_p(x,y,z)$ (Q_p is the target parameter). The nonlinear tomographic analysis of the P-wave arrival times provides a 3D P-wave velocity model as well as the raypaths from each event's hypocenter to the recording stations. Details of the velocity structure of the region from tomographic analysis is presented in Tselentis *et al.* 2007 and the picked arrival travel times measured for the velocity tomography will also be used in this investigation.

In a similar process to velocity tomography, equation (3) is parameterized in discrete blocks, within which the attenuation is assumed constant (Lees and Lindley 1994). The block dimensions should be selected so that there is no sacrifice in the resolution and the area of interest is sufficiently covered by raypaths.

The linear inversion is accomplished by minimization of the reduced (τ-τ_0) rise time residuals in an iterative procedure that includes the solution of the forward and inverse problem at each step. The linearized inversion can be written in matrix notation as (Thurber 1983):

$$\mathbf{\Delta m^{est}} = \mathbf{G}^{-1}\mathbf{\Delta d} = \mathbf{R\Delta m^{true}}, \tag{4}$$

where **G** is the Jacobian matrix that contains all the partial derivatives of the reduced rise times from earthquake hypocenters to the recording seismograph, $\mathbf{m}^{\mathrm{est}}$ is the model estimate for the, $\mathbf{m}^{\mathrm{true}}$ is the real model, and **R** is the model resolution matrix. The perturbation of the model parameters $\mathbf{\Delta m}$ expresses the disturbances of the data $\mathbf{\Delta d}$, in this case the reduced rise times:

$$\mathbf{\Delta d} \approx \mathbf{G\Delta m}. \tag{5}$$

In practice, the problem of passive tomography is usually underdetermined or mixed determined. For this reason, the matrix equation (4) is solved using the damped least-squares method, which can be expressed as:

$$\mathbf{\Delta m} = \left(\mathbf{G^T G} + \varepsilon^2 \mathbf{I}\right)^{-1} \mathbf{G}^T \mathbf{\Delta d}, \tag{6}$$

where ε^2 is the damping factor and **I** is the identity matrix. The presence of the damping factor in the inversion process is a way to avoid singular or near-singular values in the inversion matrix. Its value must be selected, taking in mind, that too small values may produce solutions with low RMS error, but they produce high oscillations in the values of the adjacent cells in the model, on the other hand, higher values mean that the result remains very close to the original model as the parameter perturbations remain small.

The resolution matrix can be written using equations 4, 5 and 6 and replacing **G** with its fundamental decomposition as:

$$\mathbf{R} = \mathbf{V}\left(\frac{\mathbf{\Lambda}^2}{\mathbf{\Lambda}^2 + \varepsilon^2\mathbf{I}}\right)\mathbf{V}^T, \tag{7}$$

Where $\boldsymbol{V}$ is a matrix whose columns are coupled-parameter-space eigenvectors, $\mathbf{\Lambda}$ is the matrix of nonzero eigenvalues, and **I** is the identity matrix. The full-resolution matrix offers important information about the quality of the inversion results. Each row of **R** describes the dependence of the solution for one model parameter on the other model parameters. The Resolution Diagonal Elements of the resolution matrix **R** (RDE), is commonly used to assess solution quality. The larger the Resolution Diagonal Elements are for the model parameters, the more independent are the solutions. This in combination with the ray hit count and the Derivative Weighted Sum (DWS) can be used to assess the solution (Tselentis *et a.*; 2007). The resolution matrix can also be used to calculate the spread (Dell'aversana *et al*. 2003) in order to check the quality of the tomography results.

A checkerboard attenuation model can be used to perform synthetic modeling and inversion in order to have a better assessment of the ability of the geometry of the network and the sources to resolve the target.

GEOLOGY

The study area covers the Rio-Antirrio strait (Figure 8), which is located in the northern part of the Peloponnesus. The Corinth and Patras rifts are linked by transfer faults in the Rio-Antirrio Strait (Doutsos and Poulimenos 1992). After the Middle Miocene, the whole northwest Peloponnesus area was uplifted and extended. During this extension, three asymmetric grabens were formed: the Corinth, Rio-Antirrio, and Patras grabens.

The asymmetry of the grabens is largely induced by north-dipping master faults, which trend parallel to the coastline of the North Peloponnesus (Doutsos and Poulimenos 1992). In the Quaternary, rifting propagated westword until it reached the Rio-Antirrio graben, The Rio graben, formed by movement of pre-existing northeast-southwest trending faults, reactivated in the Pliocene (Doutsos Kontopoulos and Ferentinos 1985). Changes in predominant stress directions at this time led to the Rio graben acting as a transfer zone between the existing Patras and Corinth grabens (Tselentis and Makropoulos 1986; Doutsos Kontopoulos and Poulimenos 1988).

The three-dimensional tomographic velocity inversion in this area has been extensively studied by Tselentis *et al.* (2007). The primary structural features are the following.

The low velocity top geological layers correspond to Quaternary and Neogene sedimentary formations. The thickness of these formations in the target area is approximately 500–600 m. These are expected to have the smaller Q_p values. The Alpine Basement is characterized by limestone with $V_p>5.2$ km/s and V_p/V_s values of 1.8. This outcrops, in the northwestern part of the study area, where the limestone Klokova Mountain is located, and also in the southern part towards the Panahaikon Mountain flysch formations are present in the northern and northeastern part of the study.

RESULTS

Figure 7 shows the estimation of the initial source rise time (τ_0). The rise times of an event are fitted with a straight line using the least squares algorithm. The intercept rise time of the line is an estimate of the τ_0 value. The downside of this approach is that some of the events that do not have enough rise times picked will have to be discarded. In this investigation, events with less than 4, or in some cases, 5 picks were ignored in the inversion procedure. Another method that could be used would be to employ the Simplex downhill algorithm in order to jointly estimate τ_0 and the average Q_p from minimizing equation (3) as discribed in De Lorenzo *et al.* (2006). But in this case this approach did not work well for all events. A reason for this might be the limited range of P wave travel times that were measured due to the network geometry.

Figure 6a depicts a histogram of all the observed pulse widths in the present investigation which range from 0.02s to 0.08s with a mean around 0.05s. Figure 6b shows the corresponding histogram for the reduced values (τ-τ_0) spanning a narrower range, with the majority of values between 0.01s to 0.065s with mean value around 0.025s.

The corrected data plotted against travel time (Figure 9b) shows a decrease in standard deviation when compared with the uncorrected data (Figure 9a). This indicates that the original variance contains effects of irregularities of both initial pulse width and attenuation structure (Wu and Lees 1996). The obvious outliers have been removed from the dataset.

In order to start the inversion procedure an estimate of the Q_p must be made and an initial model constructed that will allow calculating the initial rise time residuals. As we are not interested in $\tau_{0,}$ a plot of all the measured rise times versus the travel time as well as a plot of all the corrected rise times versus the travel time (Figures 9a, b) is used to obtain a crude estimate of an average Q_p/C. The average Q_p/C from 95 events (1452 traces) yields a Q_p/C of about 102.8. The large variance of the linear fitting implies a deviation of Q_p from homogeneous Q.

These initial estimates of the Q_p/C are used for constructing a homogeneous synthetic initial Q_0 model that will include the area of interest. This model uses a grid of evenly spaced nodes with dimensions of 1 km x1 km x1 km. In order to improve the initial model for inversion, further trials and testing were conducted using a range of initial homogeneous models and doing forward modeling. The model with the lowest RMS was estimated to be the one with a Q_0 ~100 (Q_0/C~ 200). Also these values are generally in better agreement with previous results, estimated from other seismological observations in the broader area (Tselentis 1998). The best fitting homogeneous model with the smallest RMS is used as the initial model in the next steps of the inversion. Figure 10 depicts the calculated synthetic corrected rise times against the measured ones, as well as the initial residual reduced rise times (**Δd** in equation 6).

The estimation of the Jacobian matrix (**G**) is based on, a previously calculated 3D velocity model of the area, which was derived from passive seismic travel time tomography of the same dataset (Tselentis *et al.* 2007). As the number of the measured rise times is smaller than the selected travel times, the attenuation model was coarser than the velocity one. For this, the velocity field is resampled according to the new grid parameters of the attenuation model. Also using the rays traced the term $\mathbf{G}_{i,j} = \frac{1}{V_{pi}} ds_{i,j}$ is calculated for every block i of the model and every ray j.

Finally the damping value ε was chosen, based on the trade-off between model variance and data variance (Eberhart-Phillips 1986). For a range of damping values, single iteration test inversions were conducted. Examining data variance against model variance, the damping value (25) that achieved a considerable reduction of data variance with only a modest increase in model variance was selected. Next, we calculated the Q_p model of the investigated volume of the area using equation 6.

Figures 11 a,b depict several 2D cross sections across the Rio Antirrio strait cut out from the inverted 3D Q_p model. These have an almost Southeast-Northwest direction. Figure 11c shows plan views of the 3D Q_p model at various fixed depths ranging from 0 to 4 km. The data are interpolated over a 0.5 km x 0.5 km x 0.5 km grid.

In order to assess the results a checkerboard test synthetic modeling and inversion was conducted. The checkerboard was constructed taking a homogenous model with Q_p =100 and dimensions 1 km x1 km x1 km and superposing a ±10% attenuation perturbation. Also as the regularization used in the inversion does not favor the reconstruction of sharp attenuation contrasts between the blocks, one model block with the average attenuation was interjected between these blocks. The checkerboard was used in order to construct the travel times. In the reconstruction, the original 1D attenuation model was used as starting model for the inversion. The sources and hypocenters were the same as in the actual implementation. Depth slices of the inverted volume of the checkerboard test can be seen in Figure 12. From the synthetics test we can see that the best resolved areas are in the center of the volume from 0.5 - 1Km depth and up to 4Km. In higher depths the coverage is not as good and was not used. The hit count calculated in the better resolved areas was above 200, the Derivative Weighted Sum (DWS) above 800 and the Resolution Diagonal Elements (RDE) are above ~0.3 (Figure 13).

The results appear to be in agreement with existing geological information as well as with the velocity tomograms (Vp and Vp/Vs) according to Tselentis *et al.* 2007. The top part of the model is characterized by lower Q_p values. At the Rio site the low Q_p values represent Pliocene and Recent deposits. In other parts this corresponds to Quaternary and Neogene formations. The thickness of these formations in the target area is approximately 500–600 m. This is also the areas with low V_p in the velocity model. Also, shallow drilling, that reaches to 100 m below the sea bottom, indicates the presence of Quaternary formations i.e., sand and gravel, clay, silt. The sediments towards Rio appear to be thicker than those of Antirrio

In larger depths, the Q_p values are increasing, and this characterises sites where bedrock outcrops or underlies the layer of the sediments. In the northwestern part of the study area, high values represent the limestone Klokova Mountain (Figure 8). The high Q_p in the northern and northeastern part of the study area represent the flysch formations of the Pindos zone. In the southern part of the study area, these values indicate the foot of Panahaikon Mountain where limestone and radiolarites crop out.

The Rio graben and the Antirrio fault zone at the northern part of the network are prominent features of the area. The major active faults of the study area are an indication of the important role of active tectonics in the attenuation model of the upper crust. Faults in Antirrio disrupt the bedrock formations forming the small depression in the area. The faults at the Rio site define the southern boundary of the basin. The cross sections (Figure 11a) across the Rio-Antirrio axis show that, at both Rio and Antirrio, low Q anomalies correspond to thick sediments that lie in the depressions formed by the major faults.

Conclusions

Data processing of passive seismic tomography data should not to be limited to P-wave arrival picking and the evaluation of tomograpic velocity of a prospective region. It can be extended to use additional information from the recorded seismic signals and estimate the attenuation characteristics of the medium.

In this study, a method that is based on the inversion of rise times measured on a passive seismic tomography dataset and the assumption that pulse width broadening is linearly related to Q^{-1}, has been modified and applied on real data. Using a prior velocity model derived from passive seismic tomography, a 3D attenuation model of the Rio Antirrio straits area is derived. The average Q in the area is in the order of <90-100 for the upper sedimentary formations and increases at greater depths.

The attenuation information provided by the inversion of rise times can be a way to extend the information acquired from a passive seismic network and provide insight into complex relationships in both passive seismic tomography data sets and the structural and lithological interpretation of data from active seismic surveys.

Acknowledgements

We thank Aldo Vesnaver for constructive discussions during the EAGE passive seismic workshop in Cyprous. The contribution of Tim Sokos and Anna Serpetsidaki is kindly acknowledged. We would also like to acknowledge two anonymous reviewers who helped to greatly improve the present paper.

References

Blair D.P. and Spathis A.T. 1982. Attenuation of explosion generated pulse in rock masses. Journal of Geophysical Research **87**, 3885-3892.

Bourbie T., Coussy, O. and Zinszner B. 1987. Acoustics of Porous Media. pp. 324, Butterworth-Heinemann Publisher, ISBN: 0872010252.

Clawson S.R., Smith R.B. and Benz H.M. 1989. P-wave attenuation of the Yellowstone Caldera from three-dimensional inversion of spectral decay using explosion source seismic data. Journal of Geophysical Research **94**, 7205-7222.

Courboulex F., Deichmann N. and Gariel J-C. 1999. Rupture complexity of a moderate intraplate earthquake in the Alps: the 1996 M5 Epagny Annecy earthquake. Geophysical Journal International **139**, 152–160.

Deichmann N. 1999. Empirical Green's function: a comparison between pulse width measurements and deconvolution by spectral division. Bulletin of the Seismological Society of America **89**, 178-189.

De Lorenzo S., Di Grazia G., Giampiccolo E., Gresta S., Langer H., Tusa, G. and Ursino A. 2004. Source and Q_p parameters from pulse width inversion of microearthquake data in southeastern Sicily, Italy. Journal of Geophysical Research **109**, B07308.

De Lorenzo S., Filippucci M., Giampiccolo and E. Patane D. 2006. Intrinsic Q_p at Mt. Etna from the inversion of rise times of 2002 microearthquake sequence. Annals of Geophysics **49**, 1215-1234.

Dell'Aversana P., Colombo D., Buia M. and Morandi S. 2003. Velocity interface model building in a thrust belt by tomographic inversion of global offset seismic data. Geophysical Prospecting **51**, 23–35.

Doutsos T., Kontopoulos and N. Ferentinos G. 1985. Das westlische Ende des Korinth-Grabens: Jahrbuch fur Geologie und Palaontologie, Monatshefte **11**, 652-666.

Doutsos T., Kontopoulos N. and Poulimenos G. 1988, The Corinth-Patras rift as the initial stage of continental fragmentation behind an active island arc (Greece). Basin Research **1**, 177-190.

Doutsos T. and Poulimenos G. 1992. Geometry and kinematics of active faults and their seismotectonic significance in the western Corinth-Patras rift (Greece). Journal of Structural Geology **14**, 689-699.

Durham L.S. 2003. Passive seismic. Listen: Is it the next big thing?. AAPG Explorer, 127–131.

Eberhart-Phillips D. 1986. Three-dimensional velocity structure in northern California Coast Ranges, for inversion of local arrival times. Bulletin Seismological Society America **76**, 1025–1052.

Evans J.R. and Zucca J.J. 1988. Active high-resolution seismic tomography of compressional wave velocity and attenuation structure at Medicine Lace volcano, northern California Cascade Range. Journal of Geophysical Research **93**, 15,016-15,036.

Gladwin M.T. and Stacey F.D. 1974. Anelastic degradation of acoustic pulses in rock. Physics of the Earth and Planetary Interiors **8**, 332-336.

Ho-Liu P., Kanamori H. and Clayton R.W 1988. Applications of attenuation tomography to Imperial Valley and Coso-Indian Wells region, South California. Journal of Geophysical Research **93**, 10,501-10,520.

Hedlin K., Mewhort L. and Margrave G. 2001. Delineation of steam flood using seismic attenuation. 71st SEG Meeting, San Antonio, Texas, USA, Expanded Abstracts, 1592-1595.

Kapotas S., Tselentis G-A. and Martakis N. 2003. Case study in NW Greece of passive seismic tomography: A new tool for hydrocarbon exploration. First Break **21**, 37–42.

Kjartansson E. 1979. Constant Q wave propagation and attenuation. Journal of Geophysical Research **84**, 4737-4748.

Kumar G., Batzle M. and Hofmann R. 2003. Effect of fluids on attenuation of elastic waves. 73rd SEG Meeting, Dallas, Texas, USA, Expanded Abstracts, 1592-1595.

Lees I. M. and Lindley G.T. 1994. Three dimensional attenuation tomography in Loma Prieta: inversion of t* for Q. Journal of Geophysical Research **99**, 6843-6863.

Liu H.P. 1988. Effects of source spectrum on seismic attenuation measurements using the pulse broadening method. Geophysics **53**, 1520-1526.

Liu H.P., Warrick J., Westerlund B. and Kayen E. 1994. In situ measurement of seismic shear wave absorption in the San Francisco Holocene Bay Mud by the pulse-broadening method. Bulletin of the Seismological Society of America **84**, 62-75.

Martakis N., Kapotas S. and Tselentis G-A. 2006. Integrated passive seismic acquisition and methodology.Case studies. Geophysical Prospecting **54**, 1–19.

Okada Y. 1970. The difference in the duration of P and S waves from propagating faults. Journal of Physics of the Earth **18**, 193-202.

O’Neill M.E. and Healy J.H. 1973. Determination of source parameters of small earthquakes from P-wave rise time. Bulletin of the Seismological Society of America **63**, 599-614.

Pride S.R., Harris J., Johnson D.L., Mateeva A., Nihei K., Nowack R.L., Rector J., Spetzler H., Wu R., Yamomoto T., Berryman J. and Fehler M. 2003. Permeability dependence of seismic amplitudes. The Leading Edge **22**, 518-525.

Rietbrock A. 2001. P-wave attenuation structure in the fault area of the 1995 Kobe earthquake. Journal of Geophysical Research **106**, B3,4141-4154.

Sanders C.O. and Nixon L.D. 1995. S wave attenuation structure in Long Valley caldera, California, from three-component S-to-P amplitude ratio data. Journal of Geophysical Research **100**, 12395-12,404.

Sanders C. O., Ponko. C., Nixon L. D. and Schwartz E. A. 1995. Seismological evidence for magmatic and hydrothermal structure in Long Valley caldera from local earthquake attenuation and velocity tomography. Journal of Geophysical Research **100**, B5, 8311-8326.

Sarker G. and Abers G.A.1998. Deep structures along the boundary of a collisional belt, attenuation tomography of P and S waves in the Greater Caucasus, Geophysical Journal International **13**, 326-340.

Sekiguchi H., Irikura K., Iwata T., Kakehi Y. and Hoshiba M. 1996. Minute location of faulting beneath Kobe and the waveform inversion of the source process during the 1995 Hyogo-ken Nanbu, Jabpan, earthquake using strong ground motion records, Journal of Physics of the Earth **44**,473-487.

Stacey F.D., Gladwin M.T., McKavanagh B., Linde A.T. and Hastic L.M. 1975. Anelastic damping of acoustic and seismic pulses. Surveys in Geophysics **2**, 133-157.

Thurber C. H. 1983. Earthquake locations and three-dimensional crustal structure in the Coyote Lake area, central California. Journal of Geophysical Research **88**, 8226–8236.

Tselentis G.-A. and Makropoulos K. 1986. Rates of crustal deformation in the Gulf of Corinth (Central Greece) as determined from seismicity. Tectonophysics **124**, 55-66.

Tselentis G-A. 1998: Fault lengths during the Patras 1993 earthquake sequence as estimated from the pulse width of initial p-wave. Pure And Applied Geophysics **152**, 75-89.

Tselentis G-A., Serpetsidaki A., Martakis N., Sokos E., Paraskevopoulos and P. Kapotas S. 2007. Local high-resolution seismic tomography and Kohonen neural networks-Application at the Rio-Antirrio Strait, central Greece. Geophysics **72**, B 93-B 106.

Tselentis G-A., Paraskevopoulos P., Sokos E. and Martakis N. 2009. Seismic attenuation assessment in passive seismic investigations employing pulse width analysis and considering source effects. EAGE Passive Seismic Workshop, Limassol, Cyprus, 22 - 25 March 2009.

Vesnaver A., Boehm G., Madrussani G., Rossi G. and Granser H. 2000. Depth imaging and velocity calibration by 3D adaptive tomography. First Break **18**, 7, 303-312.

Vesnaver A.L., Accaino F., Bohm G., Madrussani G., Pajchel J., Rossi G. and Moro G.D. 2003. Time-lapse tomography, Geophysics, **68**, 815–823.

Winkler K. and Nur A. 1982. Seismic attenuation: effects of pore fluids and frictional sliding. Geophysics, **47**, 1-15.

Wright C. and Hoy D. 1981. A note on pulse broadening and anelastic attenuation in near surface rocks. Physics of the Earth and Planetary Interiors **25**, 1-8.

Wu H. and Lees M. 1996. Attenuation structure of Coso Geothermal area, California, from wave pulse widths. Bulletin of the Seismological Society of America **86**, 1574-1590.

Zollo A. and De Lorenzo S. 2001. Source parameters and three-dimensional attenuation structure from the inversion of microearthquake pulse width data: method and synthetic tests. Journal of Geophysical Research **106**, 16,287-16,306.

Zucca J.J., Hutchings L.J. and Kasameyer P.W. 1994. Seismic velocity and attenuation structure of the Geysers geothermal field, California. Geothermics **23**, 111-126.

CAPTIONS OF FIGURES

Figure 1. Measurements of rise time and pulse width broadening for a single event. The starting of the pulse (Solid line), the end of the rise time (dashed line) and the pulse width (dotted line) are shown.

Figure 2. Microearthquake network. Triangles depict the location of the seismographs. We also present some representative seismograms of an earthquake as was recorded by 6 stations. The rise time variation is obvious.

Figure 3. Example of multipath effect that can introduce significant error in picking the correct rise time.

Figure 4. A 3D view of the microearthquake hypocenters, selected for rise time measurements.

Figure 5. Diagram of hypocentral distance versus the rise times. Using least squares a line is fitted to the data. The slope is at 0.0028 s/km and the data have a correlation coefficient of ~0.4.

Figure 6. Histogram of the distribution of a) measured (τ) and b) reduced (τ-τ_0) rise times.

Figure 7. Rise Time estimates at various stations (numbers) versus travel time. A least-squares fit line is used to estimate τ_0. For this event $\tau_{0=}0.0053$ sec with a slope of 19.19^o.

Figure 8. Geology of Rio-Antirrio Strait region.

Figure 9. Scatter plot of pulse width versus travel time. a) raw τ measured versus travel time. b) Corrected, τ-τ_0 versus travel time. Outliers are removed from the plots. The slope of straight line fit provides an initial indicative average of Q_o.

Figure 10. Results of forward modeling for the best fitting homogeneous initial model a) the measured rise time values (blue stars) plotted over the calculated values (red circles) and b) The residual rise times $\mathbf{\Delta d}$ in equation 6.

Figure 11. Results of the Q_p Inversion including a) Profiles along which the vertical cross sections were derived, b) vertical cross sections and c) Horizontal cross sections at various depths.

Figure 12. The results of the Q_p checkerboard test inversion.

Figure 13**.** Results for ray hits count , the Derivative Weighted Sums (DWS) and the Resolution Diagonal Elements (RDE) for selected depths. The higher values indicate the better resolved areas.

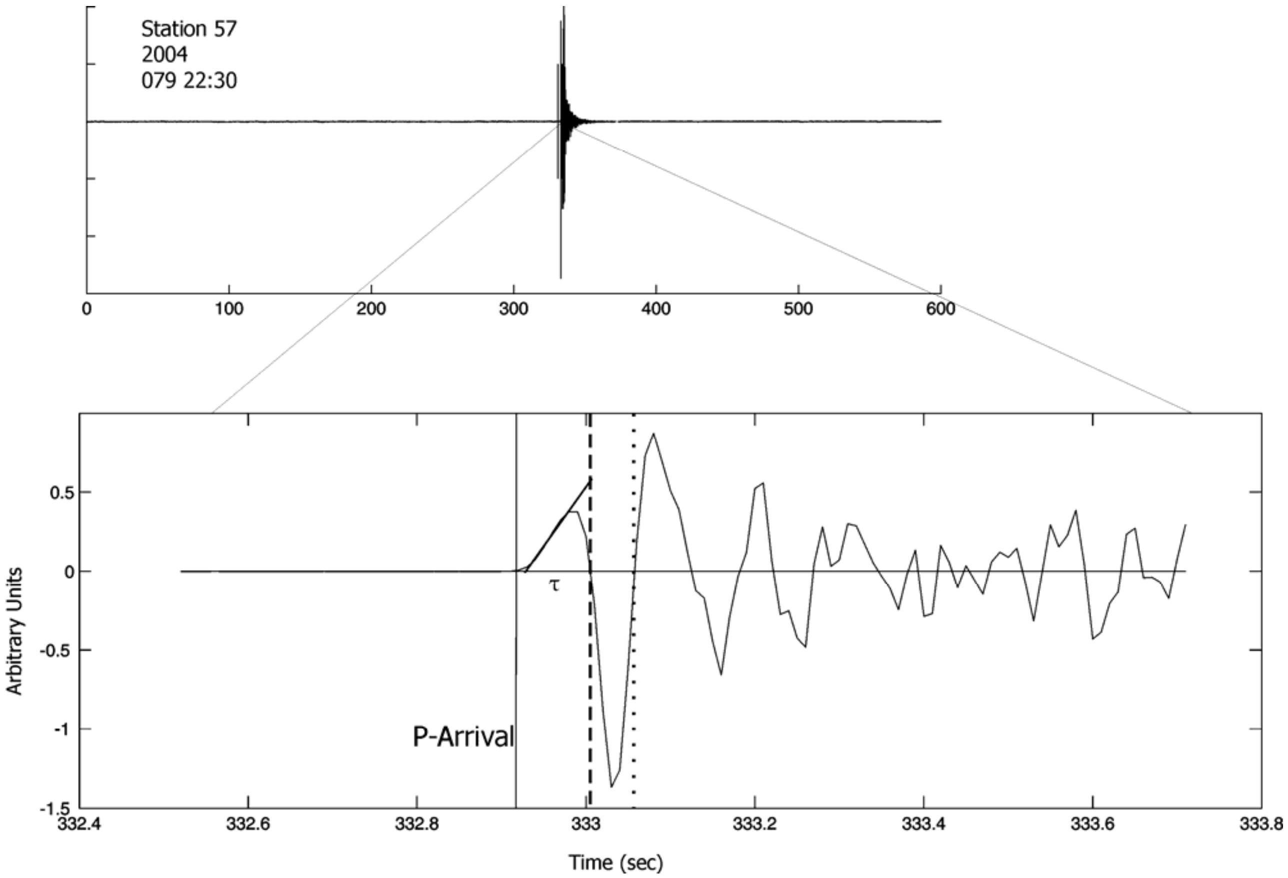
Station 57
2004
079 22:30
0
100
200
300
400
500
600
0.5
0
-0.5
-1
-1.5
Arbitrary Units
τ
P-Arrival
332.4
332.6
332.8
333
333.2
333.4
333.6
333.8
Time (sec)

FIGURE 1

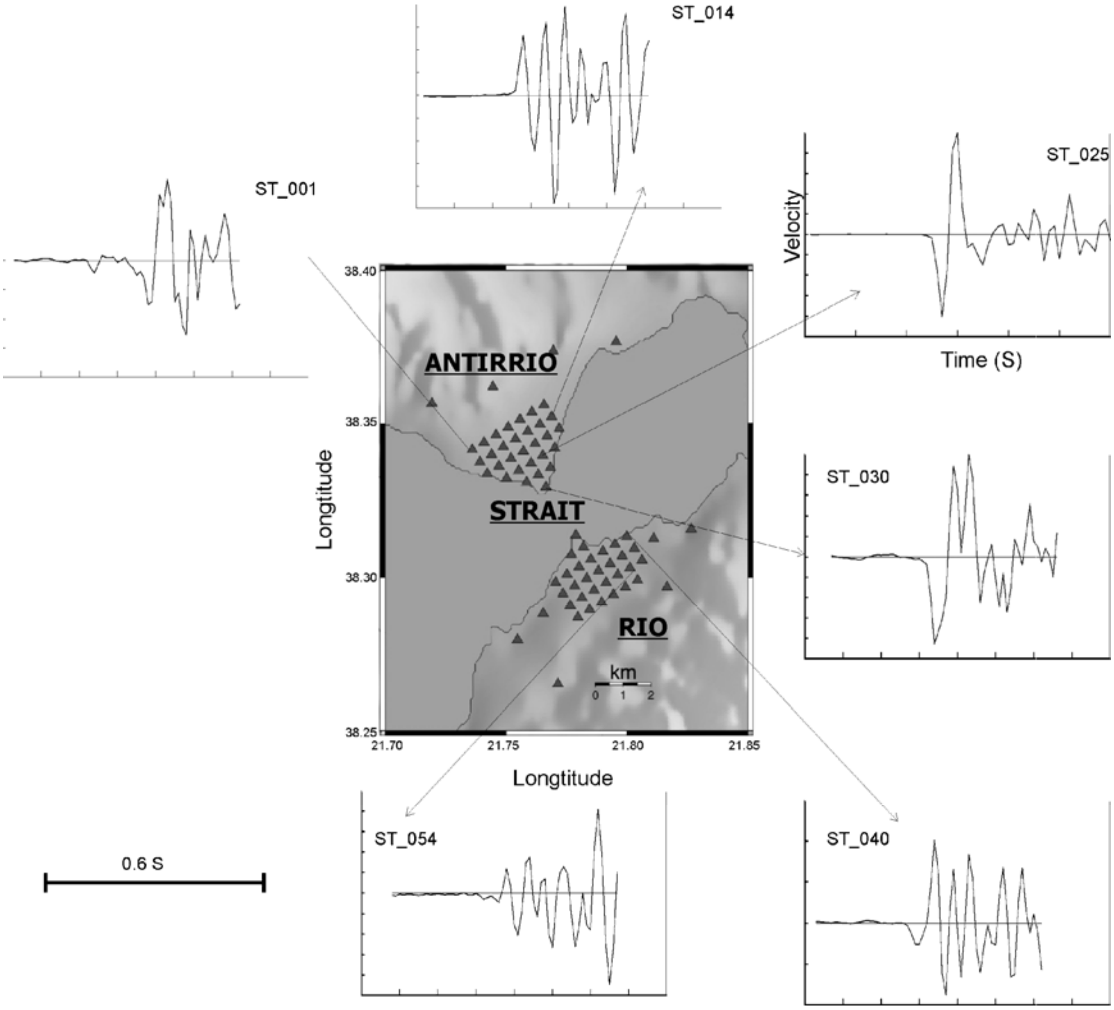
ST_014
ST_001
ST_025
Velocity
Time (S)
38.40
38.35
38.30
38.25
21.70
21.75
21.80
21.85
Longtitude
Longtitude
ANTIRRIO
STRAIT
RIO
km
0
1
2
ST_030
ST_054
ST_040
0.6 S

FIGURE 2

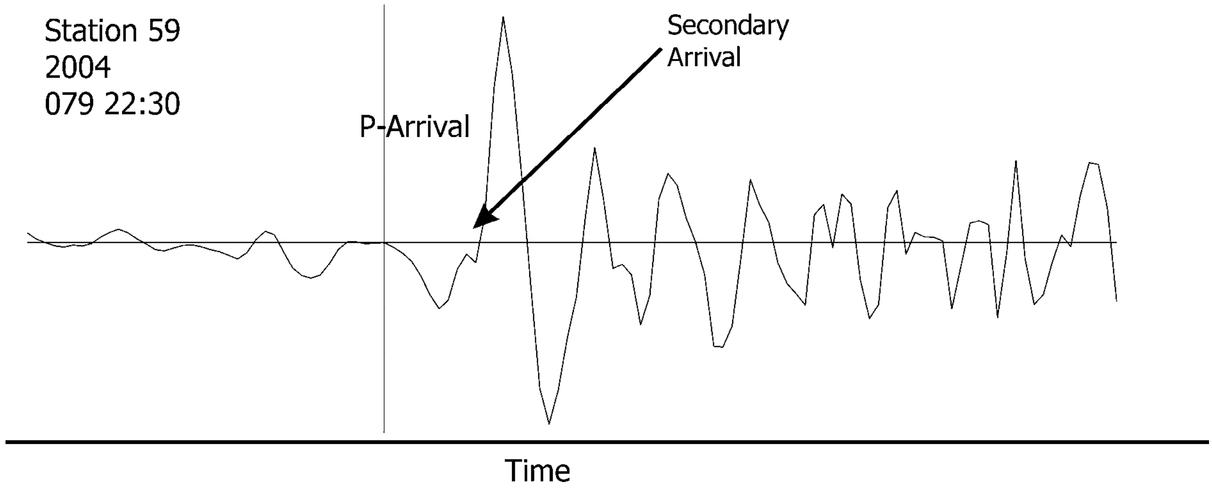

FIGURE 3

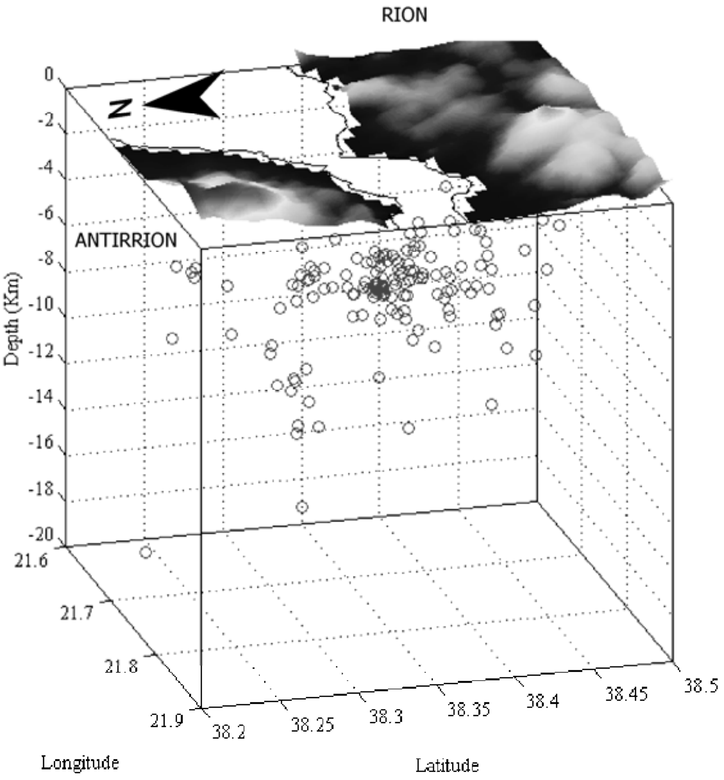
RION
ANTIRRION
N
Depth (Km)
0
-2
-4
-6
-8
-10
-12
-14
-16
-18
-20
21.6
21.7
21.8
21.9
38.2
38.25
38.3
38.35
38.4
38.45
38.5
Longitude
Latitude

FIGURE 4

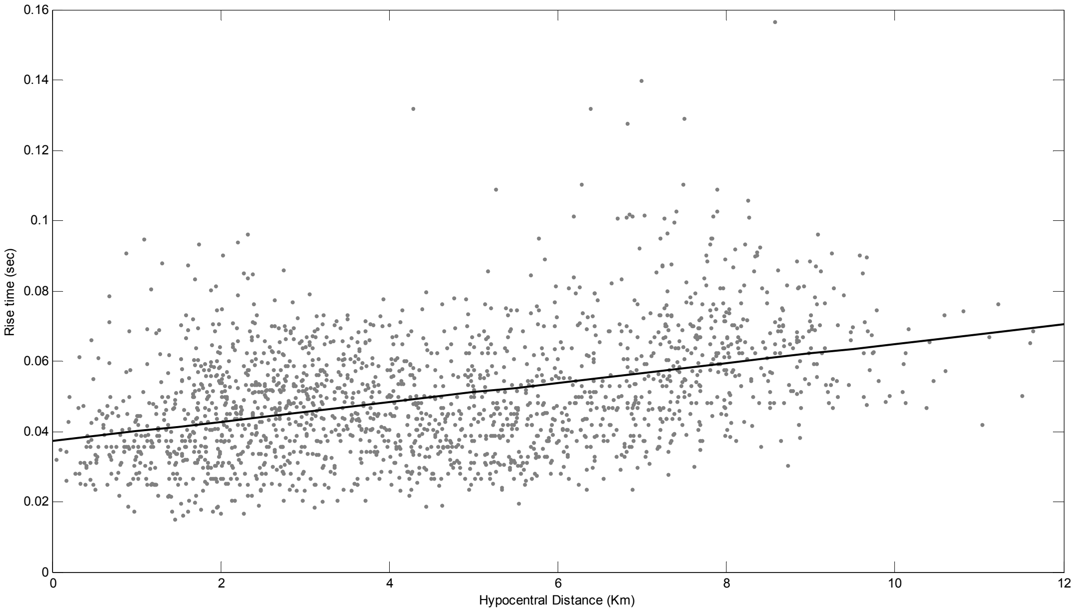
0.16
0.14
0.12
0.1
0.08
0.06
0.04
0.02
0
Rise time (sec)
0
2
4
6
8
10
12
Hypocentral Distance (Km)

FIGURE 5

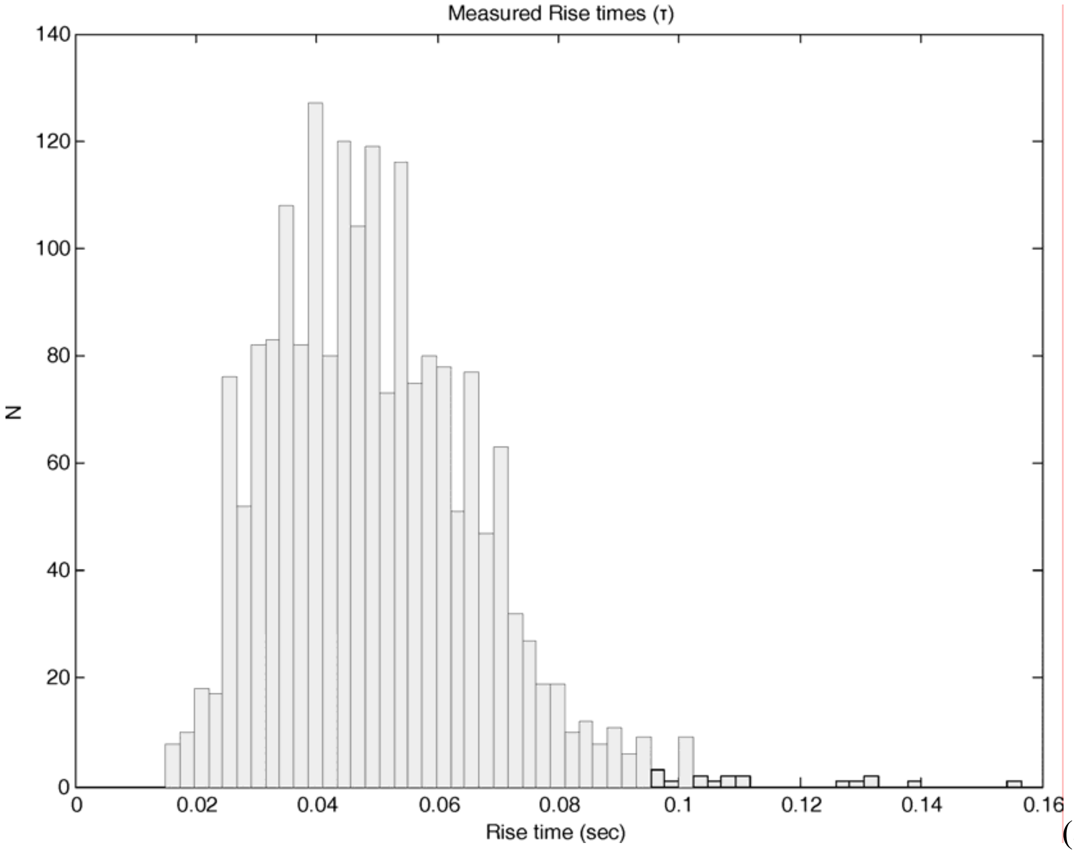
Measured Rise times (τ)
N
0
20
40
60
80
100
120
140
0
0.02
0.04
0.06
0.08
0.1
0.12
0.14
0.16
Rise time (sec)

(a)

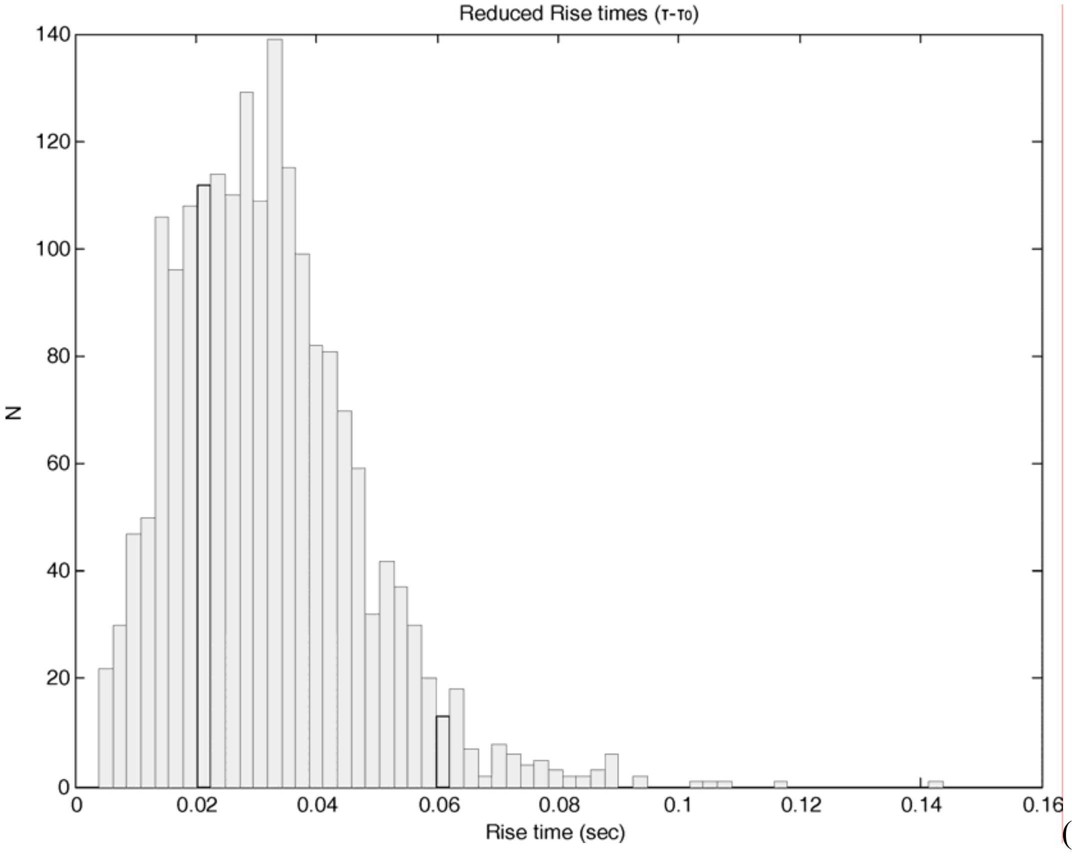
Reduced Rise times (τ-τ0)
N
0
20
40
60
80
100
120
140
0
0.02
0.04
0.06
0.08
0.1
0.12
0.14
0.16
Rise time (sec)

(b)

FIGURE 6

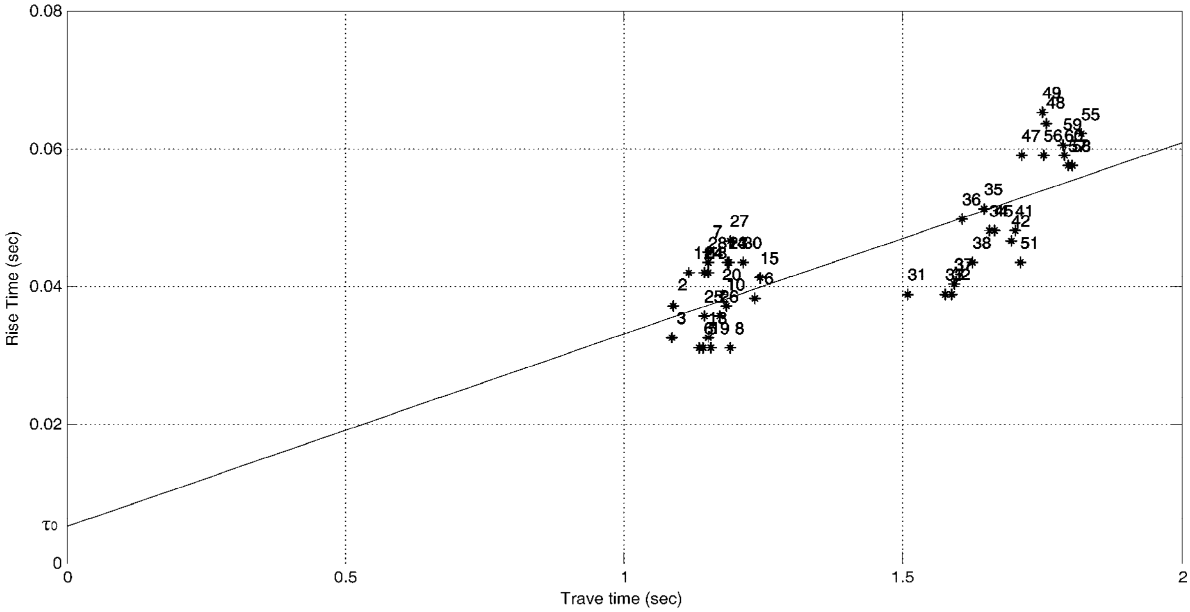
0.08
0.06
0.04
0.02
τ0
0
Rise Time (sec)
0
0.5
1
1.5
2
Trave time (sec)
27
7
15
2
20
10
6
3
8
31
36
35
41
42
38
51
37
49
48
55
59
47
56

FIGURE 7

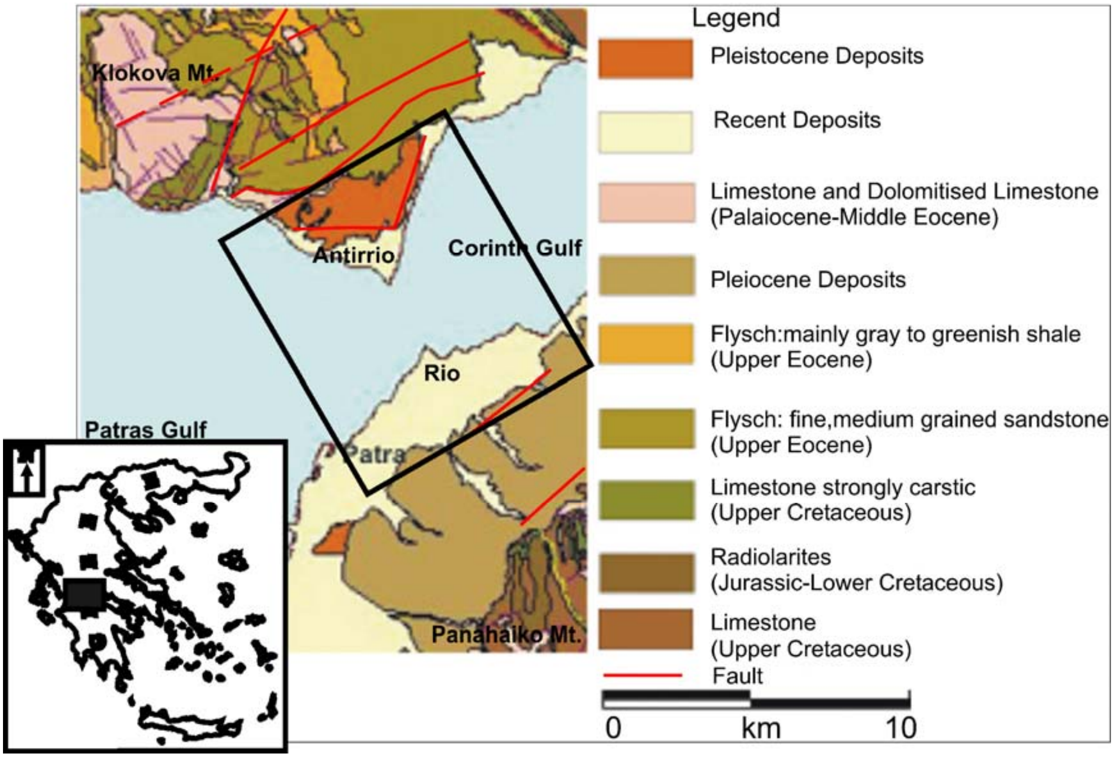
Klokova Mt.
Antirrio
Corinth Gulf
Rio
Patras Gulf
Patra
Panahaiko Mt.
Legend
Pleistocene Deposits
Recent Deposits
Limestone and Dolomitised Limestone (Palaiocene-Middle Eocene)
Pleiocene Deposits
Flysch:mainly gray to greenish shale (Upper Eocene)
Flysch: fine,medium grained sandstone (Upper Eocene)
Limestone strongly carstic (Upper Cretaceous)
Radiolarites (Jurassic-Lower Cretaceous)
Limestone (Upper Cretaceous)
Fault
0
km
10
N

FIGURE 8

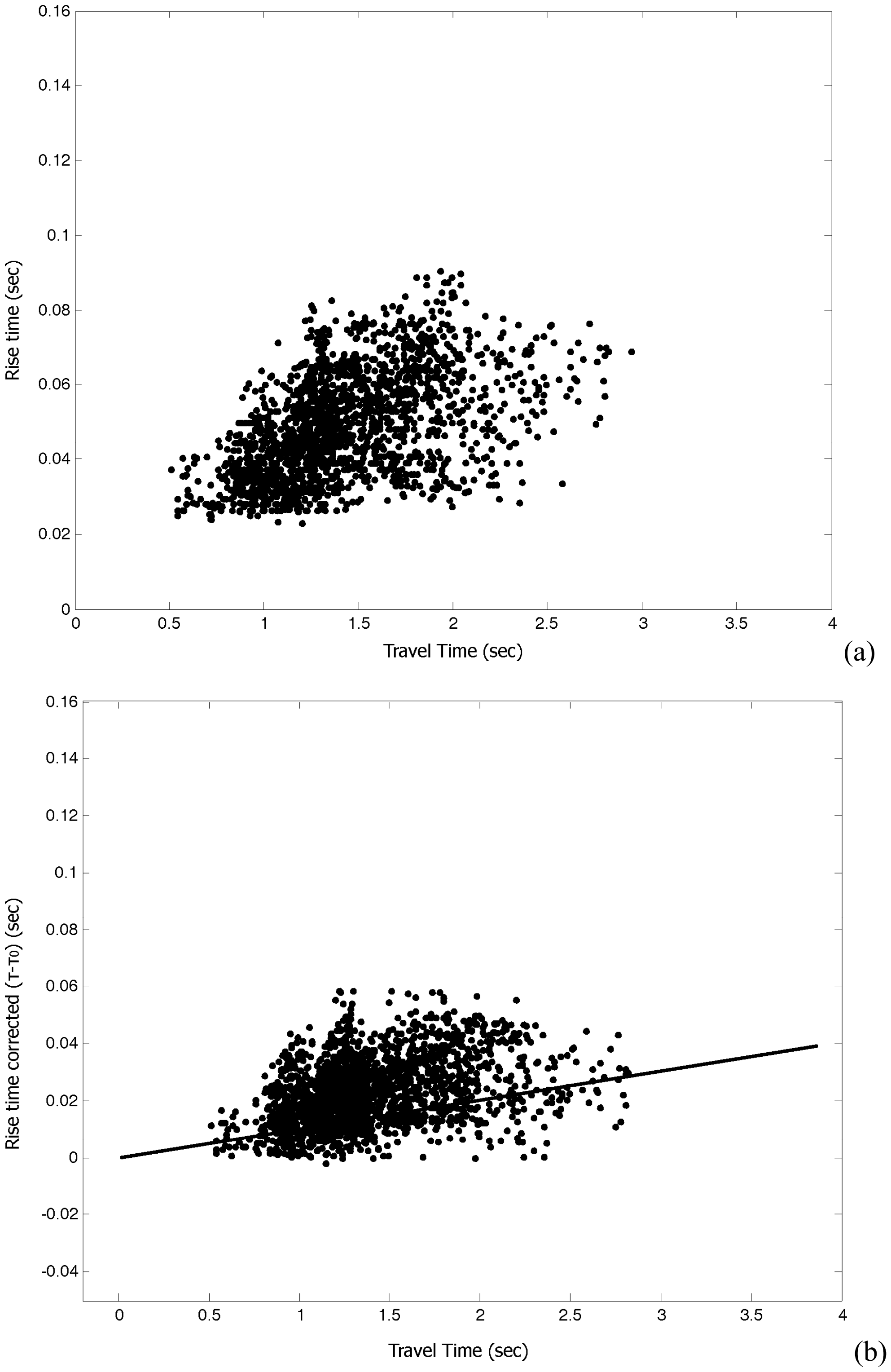

0.16
0.14
0.12
0.1
0.08
0.06
0.04
0.02
0
Rise time (sec)
0
0.5
1
1.5
2
2.5
3
3.5
4
Travel Time (sec)
(a)
0.16
0.14
0.12
0.1
0.08
0.06
0.04
0.02
0
-0.02
-0.04
Rise time corrected (T-T0) (sec)
0
0.5
1
1.5
2
2.5
3
3.5
4
Travel Time (sec)
(b)

FIGURE 9

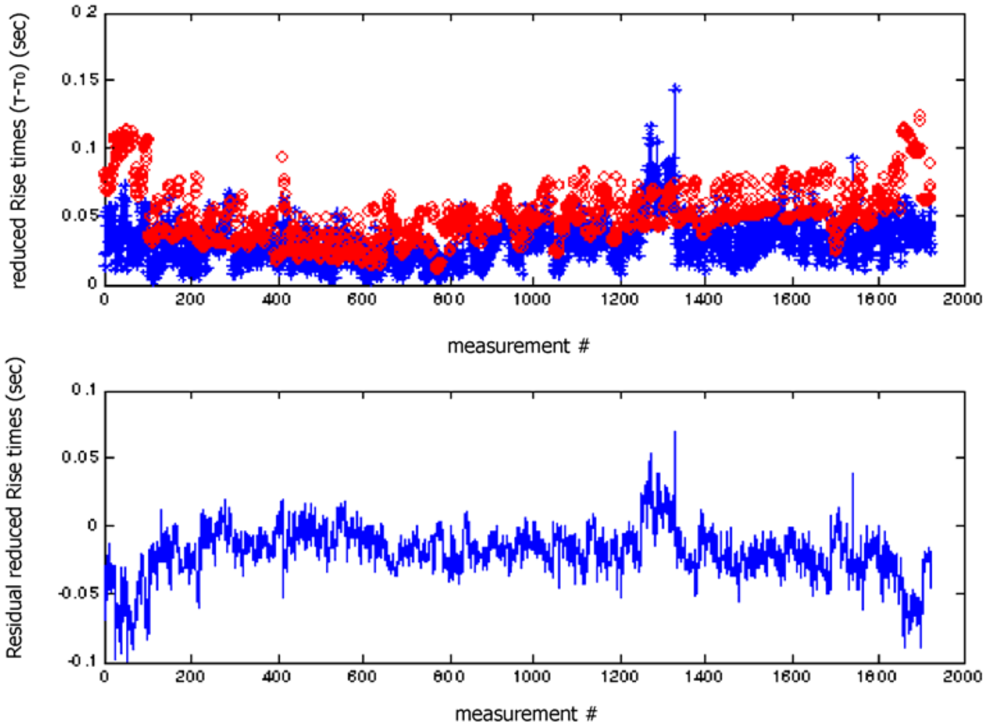
reduced Rise times (τ-τ0) (sec)
0.2
0.15
0.1
0.05
0
0
200
400
600
800
1000
1200
1400
1600
1800
2000
measurement #
Residual reduced Rise times (sec)
0.1
0.05
0
-0.05
-0.1
0
200
400
600
800
1000
1200
1400
1600
1800
2000
measurement #

FIGURE 10

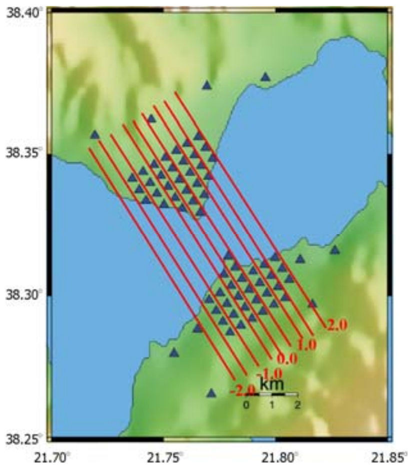
38.40°
38.35°
38.30°
38.25°
21.70°
21.75°
21.80°
21.85°
2.0
1.0
0.0
-1.0
-2.0
km
0
1
2

(a)

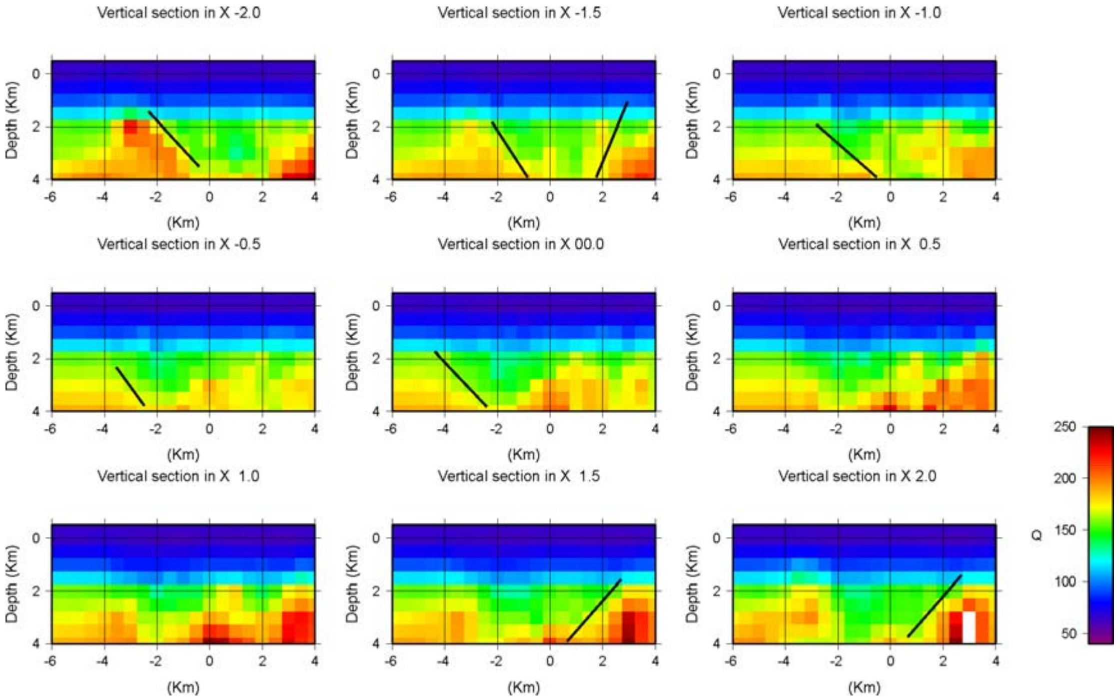
Vertical section in X -2.0
Vertical section in X -1.5
Vertical section in X -1.0
Vertical section in X -0.5
Vertical section in X 00.0
Vertical section in X 0.5
Vertical section in X 1.0
Vertical section in X 1.5
Vertical section in X 2.0
Depth (Km)
0
2
4
-6
-4
-2
0
2
4
(Km)
Q
250
200
150
100
50

(b)

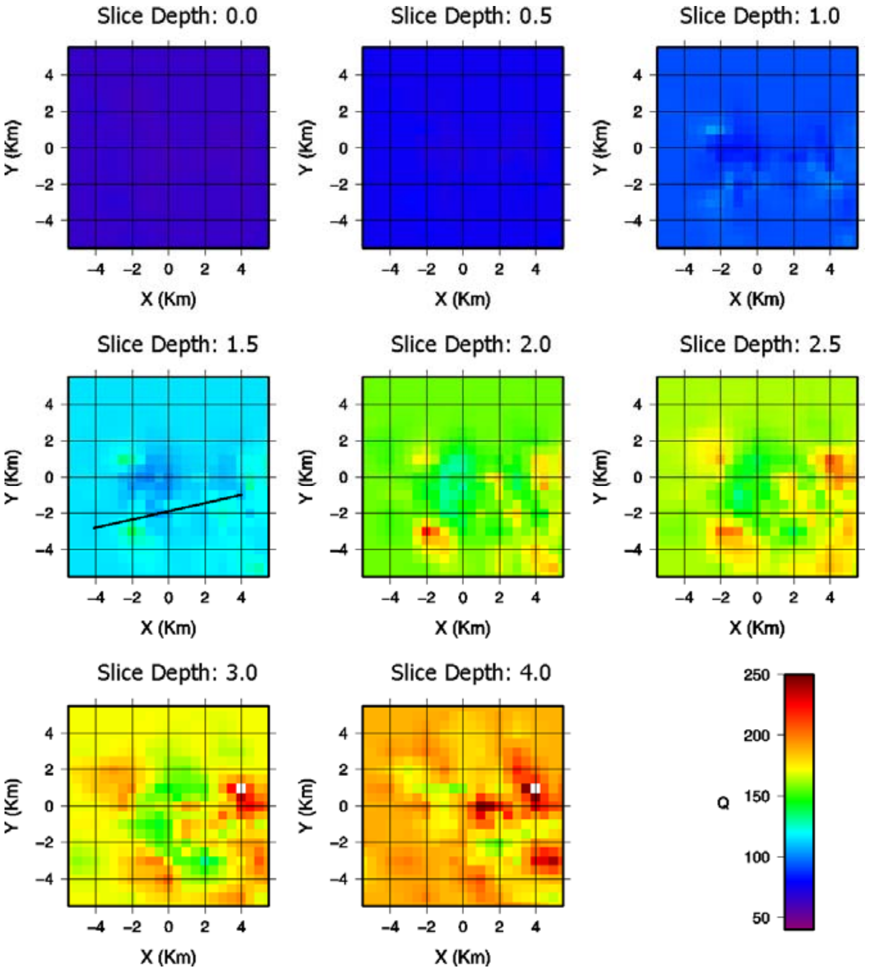

Slice Depth: 0.0
Slice Depth: 0.5
Slice Depth: 1.0
Slice Depth: 1.5
Slice Depth: 2.0
Slice Depth: 2.5
Slice Depth: 3.0
Slice Depth: 4.0
Y (Km)
X (Km)
−4
−2
0
2
4
Q
250
200
150
100
50

(c)

FIGURE 11

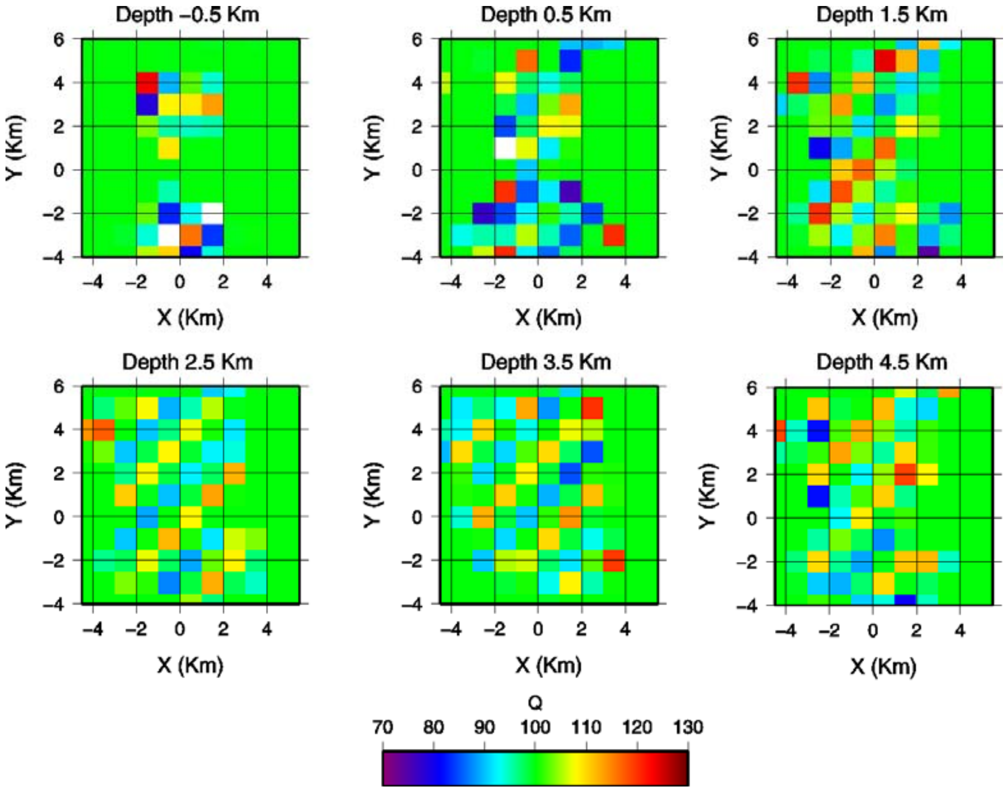
Depth −0.5 Km
Depth 0.5 Km
Depth 1.5 Km
Depth 2.5 Km
Depth 3.5 Km
Depth 4.5 Km
Y (Km)
X (Km)
6
4
2
0
−2
−4
4
Q
70
80
90
100
110
120
130

FIGURE 12:

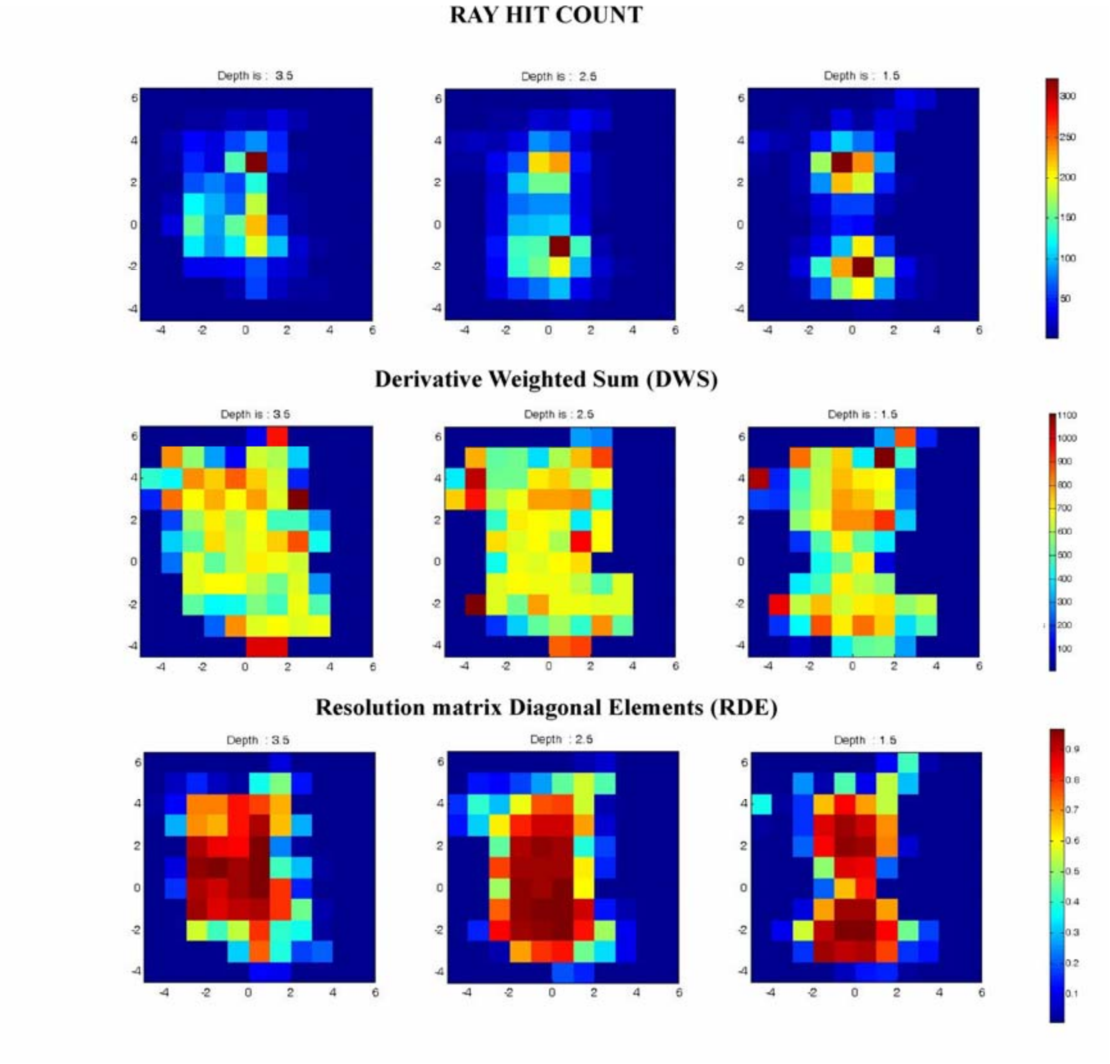

RAY HIT COUNT

Derivative Weighted Sum (DWS)

Resolution matrix Diagonal Elements (RDE)

FIGURE 13